

Anomalous electron transport in the magnetic nozzle

Shaun Andrews¹, Raoul Andriulli¹, Nabil Souhair^{1,2}, Mirko Magarotto³ & Fabrizio Ponti¹

¹ Alma Propulsion Laboratory, Department of Industrial Engineering, University of Bologna, Forlì 47122, Italy

² Lerma Laboratory Aerospace and Automotive Engineering School, International University of Rabat, Shore Rocate, Rabat 11103, Morocco

³ Department of Industrial Engineering, University of Padova, Padova 35131, Italy

E-mail: sa15339@my.bristol.ac.uk

September 2024

Abstract. This study uses fully kinetic particle-in-cell (PIC) simulation to investigate the effects of anomalous diffusion on electron transport and the propulsive performance of magnetic nozzles (MN) typical of low-power cathode-less RF plasma thrusters. The analysis provides insights into how this non-collisional transport mechanism, driven by turbulence and wave-particle interactions, influences the formation of azimuthal electron currents and, consequently, impacts thrust generation, momentum/power balance, and propulsive efficiency metrics. A Bohm-type anomalous collisionality is applied to the case of a the 150 W class REGULUS-150-Xe thruster at low (30 W) and high (150 W) operating conditions. It is found that the enhanced cross-field transport of electrons inhibits the formation of the typical MN potential barrier, reducing the radial confinement. The downstream potential drop is reduced by up to 15%. Diamagnetic electron current is diminished in the absence of steep pressure gradients and the $E \times B$ current becomes purely paramagnetic. The MN efficiency is cut from circa 0.5 to 0.2 due to loss of electron thermal energy conversion and increased plume divergence. At the Bohm limit of $\omega_{ce}/16$, agreement to experimental thrust profiles of $< 20\%$ is achieved in contrast to 48% overestimation at high-power in the classical case.

Keywords: particle-in-cell, magnetic nozzle, anomalous electron transport, Helicon plasma thruster, Bohm diffusion

Submitted to: *Plasma Sources Sci. Technol.*

1. Introduction

The magnetically enhanced plasma thruster (MEPT) is a simple low-cost electric propulsion (EP) concept, where thrust is generated by expanding an electromagnetically (EM) heated plasma through a magnetic nozzle (MN) [1, 2]. Propellant injected into a dielectric source tube is ionised and heated by a MHz range radio-frequency (RF) or GHz range microwave antenna [3]. The resulting quasi-neutral current-free plasma is then guided by a magneto-static field (in the 100-1000 G range) generated by a set of solenoids or permanent magnets [4]. Inside the source, the magnetic field confines the plasma and guides propagation of the EM waves. Outside, the discharge plasma is accelerated by diamagnetic currents interacting with the diverging magnetic field forming the MN [5]. Low-power (<250 W) devices are typically mesothermal (electron thermal velocity is greater than drift velocity) and electron-driven; namely, the heating is applied directly to the electrons [2]. These electrons have strongly magnetised gyromotion along the MN [6]; the cold ion trajectories are then determined by an ambipolar electric field that accelerates them downstream [7]. Thus, the MN radially confines the discharge, while converting electron thermal energy into directed axial ion kinetic energy, generating thrust [8]. The two main realisations of the MEPT are the RF plasma thruster [9]—which includes the Helicon Plasma Thruster (HPT) [4, 10, 11]—and the Electron Cyclotron Resonance Thruster (ECRT) [12].

The absence of plasma-immersed electrodes means MEPTs are highly resistant to erosion, which is often the lifetime-limiting aspect of conventional EP systems such as Ion and Hall effect thrusters (HET) [13]. MEPTs can also operate on a wider range of propellants, more advantageous to store for small spacecraft, and often inexpensive (e.g., iodine [14], air [15] and water) [9]. MEPTs can also be less-complex than state-of-the-art devices, since they do not require a separate dedicated neutralising electron source (e.g. a hollow cathode), which consumes power and propellant [16]. Thus, MEPTs are becoming an increasing option for low-thrust propulsion, being highly scalable, robust, light, low-cost and resistant to erosion or complex failure [17]. However, most MEPT prototypes still report thrust efficiencies lower than 20% [4].

While the main physical principles of MN's are relatively well understood, a complete description of the details of electron temperature evolution remains elusive. Measurements to date are evident that heat flux is significant in a MN expansion. Little and Choueri [18] argued that adoption of classical heat conduction, i.e. a Fourier-like law governed by collisions, can explain experimental trends in electron cooling. However, it was noted that in practice, the magnitude of the classical collision frequency was too low, which led to a nonphysical heat flux downstream greater than the power delivered to the thruster. The authors thus concluded that even if the scaling of a Fourier law is appropriate, a much higher collision frequency would be required to physically explain the expansion.

This is of particular interest, since recent experimental work has shown that plasma instabilities may be a source for enhanced, non-classical collisionality in the MN plume

[19]. Given that low temperature ($T_e < 20$ eV) MNs are typically characterised by strong cross-field gradients in potential and density, drift waves play a governing role [20]. Indeed, azimuthal plasma instabilities have been shown to lead to enhanced, “anomalous” cross-field transport in a variety of plasmas [21], including HETs, and it was recently observed that a lower hybrid drift instability in a MN plume induces an effective collision frequency several orders of magnitude higher than the classical equivalent based on standard electron-neutral or electron-ion scattering [19]. Such instabilities are driven by the large electron drift velocities in the azimuthal direction, which are often as fast as the electron thermal velocity itself, and which lead to large amplitude fluctuations in both the azimuthal electric field and the plasma density. The instabilities in axial-azimuthal HET simulations have shown frequencies in the MHz range, and electric field amplitudes almost as large as the axial accelerating field [22].

Thus, given the role of instabilities in inducing an anomalous collision frequency higher than the classical value, and the inconsistency of classical collisions in MN expansion, the need is apparent to accurately model and analyse the applicability of an anomalous collision frequency in electron transport. Indeed, cross-field transport is critically linked to the process of detachment, whereby the expanded plasma ultimately decouples from the MN [23]. Considering also that the electron heat flux directly influences the diamagnetic flow current, via the electron pressure gradient, accurate modelling of the anomalous transport is critical to giving correct numerical estimates of propulsive performance [24].

Simple phenomenological models of anomalous transport have previously been applied within a magnetised electron fluid model, where the cross-field and parallel-field anomalous collisions were accounted for separately [25]. The simulated HPT exhibited a 18% to 3% drop in thrust efficiency when anomalous cross-field collisions were near the theoretical limit. However, the role of electron transport in the fluid treatment of the MN remains limited due to the absence of self-consistent closures for non-local heat conduction. The ideal fluid model also neglects the gyro-viscous stress tensor and inertial terms, which have been shown to be significant in fully kinetic Particle-in-Cell (PIC) studies [5]. Indeed, the PIC method represents the most self-consistent numerical strategy with the lowest level of assumptions.

A multiscale numerical model for MEPTs has been recently developed, where a 0D global model [26, 27] of the source region is coupled to a 2D fully kinetic PIC model for the MN [28, 29]. While fully 3D PIC approaches are able to self-consistently capture the plasma turbulence that produces the azimuthal instabilities, 2D axisymmetric models do not consider the azimuthal direction, and thus do not include calculation of the azimuthal electric field. The scope of this work is to characterise the impact of anomalous effects on plasma transport and propulsive performance; it is therefore sufficient to make use of 2D PIC and instead include the anomalous diffusion via means of an equivalent anomalous electron scattering frequency.

This work therefore presents a first fully kinetic analysis of the effects of anomalous collisions to the electron transport in a MN (previous analysis has been preliminary

and with fluid electrons [25, 30]). To this end, the theory of anomalous transport and the relation to azimuthal current and thrust is given in section 2. Section 3 then proceeds to outline the coupled 0D global model PIC methodology, where a benchmark against independent experimental measurements is compared. Section 4 provides the results applied to a 150 W class MEPT in terms of plasma profiles, azimuthal current generation, and propulsive performance. Then, section 5 gives further insight into the role of anomalous collisionality in the electron cooling, plasma confinement, demagnetisation and detachment. Conclusions are given in section 6.

2. Methodology

2.1. Particle-in-Cell model

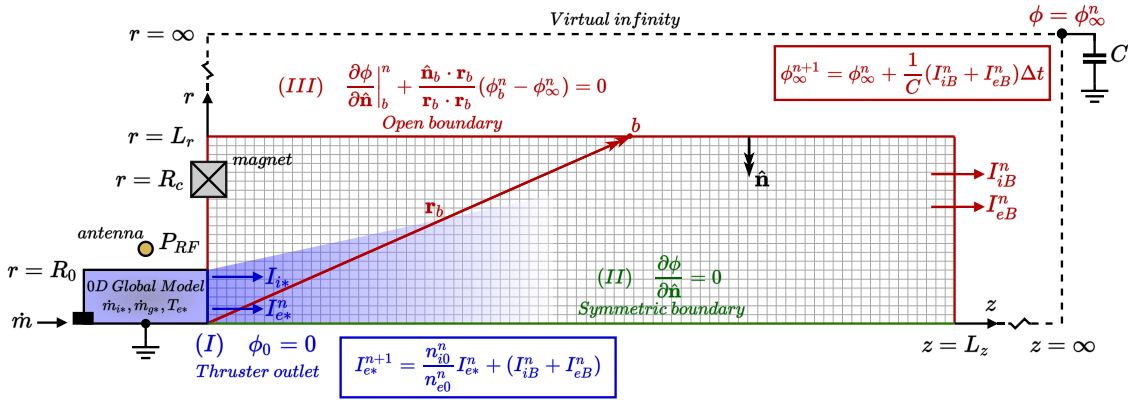


Figure 1. Simulation domain

An axisymmetric 2D3V Particle-In-Cell Direct Simulation Monte Carlo (PIC-DSMC) model [31] considers the axial z and radial r dimensions of partially-ionised plasma expansion in the MN. The simulation code is a development of that introduced extensively by Andrews et al. [28]. In this section, only an overview of the model will be given, with particular detail on the additions made to include anomalous transport. The reader is therefore referred to reference [28] for greater information.

The simulation domain is illustrated in figure 1. The plasma properties (n_{e*} , n_{g*} , T_{e*}) of the inductively coupled EM source discharge are evaluated using a 0D Global Model (GM), a complete description of which is provided in references [26, 27] and outlined in Appendix A. The GM is then coupled to the PIC model to provide the injection parameters at the thruster outlet (I), where ions, electrons and neutrals are injected. To ensure equal ion and electron current streams to the infinity at steady-state, the external boundaries (III) are treated as open to vacuum and stay connected to the thruster outlet via a virtual free-space capacitance. Boundary (II) is the axis of symmetry.

The subscripts $*$, 0 , b and ∞ shall hereby refer to, respectively, properties in the plasma source (from the GM), at the thruster outlet boundary (I), at the open

boundaries (III) and at the virtual infinity. The subscript B instead denotes the integral sum of local properties along the open boundaries.

2.1.1. Particle-in-Cell Ions i , electrons e and neutrals g are all modelled as macro-particles, with their trajectory integration performed with the *de facto* leap-frog Boris algorithm in equation (1). Jiménez et al. recently showed that >95% of deposited power is absorbed within the source tube, with <0.6% absorbed in the far-plume [32]; the EM power deposition in the MN is therefore assumed negligible and induced magnetic fields are not considered.

An explicit successive over-relaxation (SOR) Gauss-Seidel scheme solves the self-consistent plasma potential ϕ , according to the Poisson's equation of equation (2):

$$\frac{\Delta \mathbf{v}_I^{n+1/2}}{\Delta t} = \frac{q_I}{f_I m_I} (\mathbf{E}^n + \mathbf{v}_I^n \times \mathbf{B}), \quad \frac{\Delta \mathbf{r}_I^{n+1}}{\Delta t} = \mathbf{v}_I^{n+1/2} \quad (1)$$

$$\gamma^2 \varepsilon_0 \nabla^2 \phi = -\rho, \quad (2)$$

where \mathbf{r}^n is the particle position at time-step n with velocity \mathbf{v}^n , Δt is the time-step, \mathbf{E} is the electric field, and \mathbf{B} is the magneto-static field. $\rho = e(n_i - n_e)$ is the charge density, with n_i the ion density, n_e the electron density and e the elementary charge. ε_0 is the vacuum permittivity of free-space.

The constant factors $\gamma > 0$ and $f < 0$ scale the vacuum permittivity and heavy-species mass respectively for the purpose of numerical acceleration [33]. Since temporal and spatial resolution of the plasma frequency $\omega_{pe} = \sqrt{n_e e^2 / \varepsilon_0 m_e}$ and Debye length $\lambda_D = \sqrt{\varepsilon_0 k_B T_e / n_e e^2}$ is required, the permittivity scaling increases both mesh size and time-step by γ . The final result is a simulation speed-up of approximately $\gamma^2 \sqrt{f}$. A more detailed description of the acceleration scheme and a sensitivity analysis on the values of γ and f used in the PIC model can be found in reference [28]. At each time-step, the electric field is then updated per the electrostatic relation $\mathbf{E} = -\nabla \phi$.

2.1.2. Boundary Conditions The thruster outlet (I) is given the reference potential $\phi_0 = 0$. A zero-Neumann condition ($\partial \phi / \partial \hat{\mathbf{n}} = 0$) is applied to the symmetric $r = 0$ boundary (II). At the open boundaries (III), the non-stationary Robin condition, established by Andrews et al. [28], is used:

$$\left. \frac{\partial \phi}{\partial \hat{\mathbf{n}}} \right|_b^n + \frac{\hat{\mathbf{n}}_b \cdot \mathbf{r}_b}{\mathbf{r}_b \cdot \mathbf{r}_b} (\phi_b^n - \phi_\infty^n) = 0, \quad (3)$$

where \mathbf{r}_b is the vector from the centre of the thruster outlet (I) to a location on the open boundary (III), $\hat{\mathbf{n}}$ is the inward-pointing unit normal, and ϕ_∞ denotes the free-space plasma potential at infinity.

At the thruster outlet (I), particles with a generalised Maxwellian distribution are injected each time step:

$$f_I^+(\mathbf{v}_I) = \sqrt{\frac{m_I}{2\pi k_B T_{I*}}} \exp\left(-\frac{m_I}{2k_B T_{I*}} |\mathbf{v}_I - \mathbf{u}_I|^2\right) H(v_{Iz}) \quad (4)$$

where T_{I^*} is the source reference species temperature. The drift velocity \mathbf{u}_I , imposed in the z direction, is equal to the Bohm speed for ions and electrons: $\mathbf{u}_{i,e} = \langle c_*, 0, 0 \rangle$, where $c_* = \sqrt{k_B T_{e^*} / m_i}$. Neutrals instead possess thermal drift velocity $\mathbf{u}_g = \langle \bar{v}_g / 4, 0, 0 \rangle$, where $\bar{v}_g = \sqrt{8k_B T_{g^*} / \pi m_g}$. $H()$ is the Heaviside function, since only forward-marching distributions ($v_{Iz} > 0$) can be imposed.

Ions, electrons and neutrals returning to the thruster outlet are absorbed, as are ions and neutrals reaching the open boundaries. For electrons at the open boundaries, an energy-based reflection criterion accounts for the trapped population returned by the ambipolar potential drop. The kinetic energy of electrons KE_e is compared to the trapping potential PE_b on the boundary node,

$$KE_e = \frac{1}{2} m_e |\mathbf{v}_e|^2 \quad (5)$$

$$PE_b = e(\phi_b - \phi_\infty). \quad (6)$$

If $KE_e < PE_b$ the electron is trapped, so is reflected back with velocity $-\mathbf{v}_e$. Else, it is a free electron to be removed from the domain.

From this energy-based criterion, there is a value of ϕ_∞ that reflects the number of electrons required for a global current-free plume. Therefore, ϕ_∞ is self-consistently controlled via a virtual free-space capacitance C ,

$$\phi_\infty^{n+1} = \phi_\infty^n + \frac{1}{C} (I_{iB}^n + I_{eB}^n) \Delta t, \quad (7)$$

where I_{iB} and I_{eB} are the sum ion and electron currents leaving the open boundaries (III). The ion and electron currents streaming to infinity are therefore equal at steady-state.

To complete the circuit, any non-zero net current leaving the open boundaries (III) during the transient must be injected back into the domain through the thruster outlet (I). The injected electron current I_{e^*} is further controlled in order to enforce quasi-neutrality. While ions are injected with a constant current given by $I_{i^*} = en_{i^*} c_* A_0$, where A_0 is the area of the thruster outlet, the injected electron current is updated each time step according to

$$I_{e^*}^{n+1} = (I_{iB}^n + I_{eB}^n) + \frac{n_{i0}^n}{n_{e0}^n} I_{e^*}^n, \quad (8)$$

where the first term completes the circuit and the second term sustains quasi-neutrality. Since the injected electrons are Maxwellian, the initial current is $I_{e^*}^0 = -en_*(\bar{v}_{e^*}/4 + c_*)A_0$. The injected neutral thermal flux is then $\Gamma_{g^*} = n_{g^*} \bar{v}_{g^*} A_0 / 4$.

In conclusion, there exists a fully-consistent coupling between the current from the plasma source $I_{i0} = -I_{e0}$ to the open boundaries $I_{iB} = -I_{eB}$, the potential drop ϕ_∞ and the macroscopic plume solution. It is upheld via the boundary condition of equation (3), the electron energy reflection condition, and the capacitive circuit control of equation (7) and equation (8).

2.1.3. Classical collisions The simulation takes into account Coulomb collisions, ion-neutral scattering, charge exchange collisions, and electron-neutral elastic and inelastic scattering. Intra-species collisions are treated using the complete Direct Simulation Monte Carlo (DSMC) technique [34], while inter-species collisions are handled using the Monte Carlo Collision (MCC) methodology [35]. Regarding the ionisation interaction, only first ionisation has been considered. Data about the employed collision cross-sections is obtained from source [33].

In order to limit the computational time, the electron-neutral inelastic excitation reactions have been lumped in 2 different states, 1S and 2P as introduced in [26]. The excited states are not modelled, hence, after the collision, particles are assumed to immediately decay to the ground state. As a consequence, electron-neutral excitation interactions act as an energy sink for electrons.

2.1.4. Anomalous collisions The model of the anomalous collision frequency is crucial for the resulting plasma dynamics. In the previous decade, many attempts have been made to find accurate, flexible and self-consistent models. The empirical Bohm model [36] is based on the idea that anomalous Bohm diffusion results in the additional electron mobility observed experimentally. The theory behind the mechanism for Bohm diffusion, presented by Esipchuck et al. [37], considers that the azimuthal drift waves can exist only in regions with decreasing gradients in the magnetic field. The anomalous collision frequency is

$$\nu_{an} = \alpha_{an}\omega_{ce} \quad (9)$$

where α_{an} is an empirical coefficient and $\omega_{ce} = q|\mathbf{B}|/m_e$ is the local electron gyro-frequency. In the fully-turbulent limit, $\alpha_{an} = 1/16$, though studies of HETs have found best-fit values in the range $10^{-3} - 1$ [21]. The MCC probability of an anomalous collision event is then

$$P_{an} = 1 - \exp(-\nu_{an}\Delta t) \quad (10)$$

If a collision occurs, electrons are assumed to scatter preferably in the direction perpendicular to the magnetic field [38]. Therefore, the post-collision velocity \mathbf{v}'_e is derived by rotating the perpendicular component of the electron velocity vector $\mathbf{v}_{e\perp}$ with respect to \mathbf{B} with an arbitrary angle $\psi = 2\pi\mathcal{R}[0, 1]$, where $\mathcal{R}[a, b]$ is a random number between a and b , and leaving the parallel component unchanged.

$$\mathbf{v}'_e = \underbrace{(\mathbf{v}_e \cdot \hat{\mathbf{b}}) \hat{\mathbf{b}}}_{\mathbf{v}_{e\parallel}} + \mathbf{Q}_{\perp}(\psi) \underbrace{(\mathbf{v}_e - (\mathbf{v}_e \cdot \hat{\mathbf{b}}) \hat{\mathbf{b}})}_{\mathbf{v}_{e\perp}} \quad (11)$$

where

$$\mathbf{Q}_{\perp}(\psi) = \begin{bmatrix} \cos(\psi) & 0 & \sin(\psi) \\ 0 & 1 & 0 \\ -\sin(\psi) & 0 & \cos(\psi) \end{bmatrix} \quad (12)$$

is the perpendicular rotation matrix and $\hat{\mathbf{b}} = \mathbf{B}/|\mathbf{B}|$.

2.2. Electron transport

The parameters discussed in the following are calculated in post-processing as moments of the distribution functions provided by the PIC model [38].

2.2.1. Momentum, azimuthal current and thrust At steady-state, the first integral moment of the electron velocity distribution function fulfills the momentum equation [39],

$$\mathbf{0} = en_e(\mathbf{E} + \mathbf{u}_e \times \mathbf{B}) + \nabla \cdot (p_e \bar{\mathbf{I}} + \bar{\boldsymbol{\pi}}_e + m_e n_e \mathbf{u}_e \mathbf{u}_e) - \mathbf{R}_e - \mathbf{R}_{an}, \quad (13)$$

where: \mathbf{u}_e is the electron macroscopic drift velocity; the (symmetric) pressure tensor

$$\bar{\mathbf{P}}_e \equiv m_e \int \mathbf{w}_e \mathbf{w}_e f_e(\mathbf{v}_e) d\mathbf{v}_e = p_e \bar{\mathbf{I}} + \bar{\boldsymbol{\pi}}_e, \quad (14)$$

with $\bar{\mathbf{I}}$ the identity tensor and $\mathbf{w}_e = \mathbf{v}_e - \mathbf{u}_e$, has been split into the scalar static isotropic part $p_e = \frac{1}{3} \text{tr}(\bar{\mathbf{P}}_e) = k_B n_e T_e$ and the anisotropic viscosity tensor $\bar{\boldsymbol{\pi}}_e$; $\mathbf{R}_e \equiv \mathbf{R}_{ei} + \mathbf{R}_{en}$ is the resistive collisional friction force density due to electron collisions with species $k = i, n$

$$\mathbf{R}_e = - \sum_k m_{ek} n_k (\mathbf{u}_e - \mathbf{u}_k) \nu_{ek} \quad (15)$$

with ν_{ek} the collision frequency and $m_{ek} = m_e m_k / (m_e + m_k)$ the reduced mass; the anomalous term \mathbf{R}_{an} can be considered an equivalent instability-enhanced electron-ion friction force density,

$$\mathbf{R}_{an} = -m_e n_e (\mathbf{u}_e - \mathbf{u}_i) \bar{\boldsymbol{\nu}}_{an} \quad (16)$$

where $\bar{\boldsymbol{\nu}}_{an}$ is the diagonal anomalous collision frequency tensor—written in this form only to imply that it is not necessarily isotropic—and where $\mathbf{1}_\theta \cdot \bar{\boldsymbol{\nu}}_{an} \cdot \mathbf{1}_\theta = \nu_{an}$. The anomalous axial and radial collision frequency is instead obtained from the conductivity tensor $\bar{\boldsymbol{\sigma}} = \frac{n_e e^2}{m_e} \cdot (\bar{\boldsymbol{\nu}}_{an}^{-1} + \nu_e^{-1})$ [39], which is obtained from Ohm's law $\mathbf{j}_e = \bar{\boldsymbol{\sigma}}(\mathbf{E} + \mathbf{u}_e \times \mathbf{B})$.

In a mesothermal plasma (i.e. $\mathbf{u}_e \ll \mathbf{v}_{th,e}$) the inertial component of the substantive derivative can be considered negligible ($\nabla \cdot (m_e n_e \mathbf{u}_e \mathbf{u}_e) \sim 0$). The total flow components are then obtained by taking the cross product of the momentum equation with the magnetic field \mathbf{B} :

$$\mathbf{u}_e = \frac{(\mathbf{B} \cdot \mathbf{u}_e) \mathbf{B}}{|\mathbf{B}|^2} + \frac{\mathbf{E} \times \mathbf{B}}{|\mathbf{B}|^2} + \frac{\nabla p_e \times \mathbf{B}}{en_e |\mathbf{B}|^2} + \frac{\nabla \cdot \boldsymbol{\pi}_e \times \mathbf{B}}{en_e |\mathbf{B}|^2} + \frac{\mathbf{R}_e \times \mathbf{B}}{en_e |\mathbf{B}|^2} + \frac{\mathbf{R}_{an} \times \mathbf{B}}{en_e |\mathbf{B}|^2} \quad (17)$$

The first term in equation (17) is the parallel flow velocity $\mathbf{u}_\parallel = \mathbf{u}_e \cdot \mathbf{B} / |\mathbf{B}|$. Making use of the fact that $\mathbf{u}_\parallel \cdot \mathbf{1}_\theta = 0$, the azimuthal electron current density $j_{e\theta}$ is then

$$j_{e\theta} = -en_e u_{e\theta} = - \left[\underbrace{en_e \frac{\mathbf{E} \times \mathbf{B}}{|\mathbf{B}|^2}}_{E \times B} + \underbrace{\frac{\nabla p_e \times \mathbf{B}}{|\mathbf{B}|^2}}_{\text{Diamagnetic}} + \underbrace{\frac{\nabla \cdot \boldsymbol{\pi}_e \times \mathbf{B}}{|\mathbf{B}|^2}}_{\text{Stress}} + \underbrace{\frac{\mathbf{R}_e \times \mathbf{B}}{|\mathbf{B}|^2}}_{\text{Friction}} \right] \cdot \mathbf{1}_\theta. \quad (18)$$

In equation (18), the terms on the right-hand side correspond to the contributions due to the $\mathbf{E} \times \mathbf{B}$ drift $j_{e\theta}^{E \times B}$, diamagnetic flow $j_{e\theta}^\chi$, gyro-viscous stress $j_{e\theta}^\pi$, and classical friction $j_{e\theta}^f$ respectively.

The total axial momentum flux F (thrust) of the plasma expansion is

$$F = \oint_{S(V)} \sum_{k=i,e,g} \mathbf{1}_z \cdot \left(m_k n_k \mathbf{u}_k \mathbf{u}_k + p_k \bar{\bar{\mathbf{I}}} + \bar{\bar{\boldsymbol{\pi}}}_k \right) \cdot \hat{\mathbf{n}} dS \quad (19)$$

where S is the bounding surface of the simulation control volume V . Considering the summation of the electron momentum equation with its ion and neutral counterparts, the thrust can also be expressed by

$$F = F_0 + \iiint_V -j_{e\theta} B_r dV \quad (20)$$

where F_0 is the axial force entering the MN from the plasma source [40]. The integrand term can be considered as the Lorentz force density, and can be separated into the same contributions as described for $j_{e\theta}$ in equation (18) (note that ion azimuthal current is negligible). This can be decomposed into the azimuthal current contributions listed in equation (18),

$$F_{E \times B} = \iiint_V -j_{e\theta}^{E \times B} B_r dV, \quad (21)$$

$$F_\chi = \iiint_V -j_{e\theta}^\chi B_r dV, \quad (22)$$

$$F_\pi = \iiint_V -j_{e\theta}^\pi B_r dV, \quad (23)$$

$$F_f = \iiint_V -j_{e\theta}^f B_r dV. \quad (24)$$

2.2.2. Power and efficiency The steady-state energy equation for each species k is obtained by taking the energy moment of the kinetic equation [39]:

$$\mathbf{0} = \nabla \cdot \left[\mathbf{q}_k + \left(\frac{5}{2} k_B n_k T_k + \frac{1}{2} n_k m_k |\mathbf{u}_k|^2 \right) \mathbf{u}_k + \mathbf{u}_k \cdot \bar{\bar{\boldsymbol{\pi}}} \right] - n_k q_k \mathbf{u}_k \cdot \mathbf{E} - U_k - \mathbf{u}_k \cdot \mathbf{R}_k - \Psi_k \quad (25)$$

The divergence term includes the sum of the net energy flux densities into the local volume due to heat conduction \mathbf{q} , heat convection, macroscopic kinetic, and dissipation due to flow-gradient-induced stress respectively. The second term is the electric field energy. The remaining terms account for the work done by collisional heat-exchange U , momentum exchange, and inelastic collision energy losses such as ionisation and excitation Ψ [41].

Taking the volume integral of equation 21, the terms of the MN power balance $P_* = \sum_k (P_{kin,k} + P_{P,k} + Q_k) - P_{loss}$ can be defined as:

$$P_{kin,k} = \int_S \left[\frac{1}{2} n_k m_i |\mathbf{u}_k|^2 \mathbf{u}_k \right] \cdot \hat{\mathbf{n}} dS, \quad (26)$$

$$P_{P,k} = \int_S \left[\frac{5}{2} n_k T_k \mathbf{u}_k + \mathbf{u}_k \cdot \overline{\overline{\boldsymbol{\pi}}}_k \right] \cdot \hat{\mathbf{n}} dS, \quad (27)$$

$$Q_k = \int_S \mathbf{q}_k \cdot \hat{\mathbf{n}} dS, \quad (28)$$

$$P_{loss} = \int_V \sum_k (U_k + \mathbf{u}_k \cdot \mathbf{R}_k + \Psi_k) dV, \quad (29)$$

$$P_* = \sum_k [P_{kin,k}(0) + P_{P,k}(0) + Q_k(0)]. \quad (30)$$

These are the macroscopic kinetic energy flux, total pressure energy flux, heat flux, collisional loss power and the total power entering the MN respectively. Power-related efficiencies of interest are the energy conversion efficiency, the ion divergence efficiency and the total MN efficiency, which can then be defined as:

$$\eta_{ene} = \frac{P_{kin,i}}{P_*}, \quad \eta_{div} = \frac{P_{kin,i}^{(z)}}{P_{kin,i}}, \quad \eta_{MN} = \frac{\sum_k (P_{kin,k}^{(z)} + P_{P,k})}{P_*}. \quad (31)$$

The superscript (z) refers to the axial component of the kinetic power. These efficiencies represent the effectiveness of electron thermal to ion kinetic energy conversion, plume confinement, and overall MN thrust generation [2]. The typical thrust efficiency can be given as

$$\eta_F = \frac{F^2}{2\dot{m}P_a} \approx \eta_s \eta_{MN}, \quad (32)$$

where $\eta_s = P_*/P_a$ is the source efficiency provided by the global model (see Appendix A).

3. Independent benchmark validation

Although the PIC model has been validated previously [28] with the measurements of Lafleur et. al. [10], the magnetic field was too weak ($B_0 \approx 40$ G) for the anomalous transport to be significant compared to classical collisions. The experimental results from the RF thruster of Little and Choueiri [18] have become a *de facto* benchmark for MN simulations [42, 43]. The measurements shown in figure 2 were gathered for an Argon mass flow rate of $\dot{m} = 0.5$ mg/s, into a source tube of diameter 75 mm and length 305 mm, with the power delivered to the antenna of approximately 500 W; the MN throat strength was $B_0 \approx 370$ G. This resulted in reference properties of $n_{e*} \approx 10^{18}$ m⁻³ and $T_{e*} \approx 7$ eV. A swept RF-compensated Langmuir probe (LP) measured the plasma density and electron temperature; the plasma potential was obtained with a heated emissive probe (EP) using the floating point method; the ion velocity the ion energy distribution function measured with a four-grid retarding potential analyzer (RPA). The

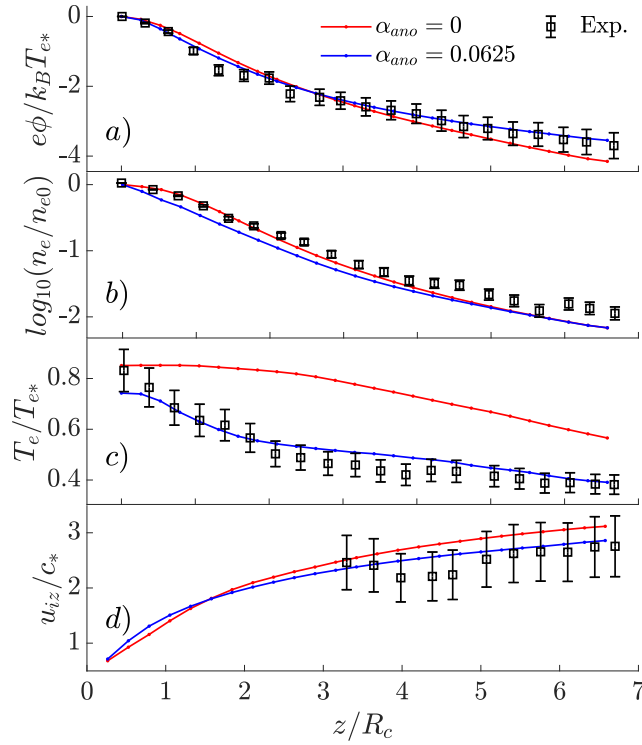


Figure 2. Benchmark validation of the PIC model, with anomalous transport, against the experimental data measured by Little and Choueiri [18].

uncertainty bands associated to the LP are 5% and 10% for density and temperature respectively. The error of the EP is 5%, and the RPA 25%.

The comparisons of the simulated and measured properties along the MN axis are presented in figure 2, where both classical and fully-turbulent anomalous transport ($\alpha_{an} = 1/16$) have been considered. There is excellent agreement in the fully-turbulent case, particularly in the plasma potential of figure 2 (a), ion axial velocity figure 2 (d), and electron temperature figure 2 (c), where the classical transport model fails to capture the rapid cooling seen experimentally. However, it must be acknowledged that the electron density profile of figure 2 (b) has increased discrepancy in the fully-turbulent case, but the error is still $< 15\%$. The reasons for this are most likely the omission of vacuum chamber wall effects or the assumption of a spatially uniform α_{an} . Nevertheless, the model represents the physical process well, generally within the errorbars of all measurements.

4. Results

4.1. Thruster description and numerical setup

4.1.1. *150 W MEPT* The thruster analysed in this work is a particular configuration of the low-power 150 W class MEPT ‘REGULUS-150’, described in references [44, 45, 46]. The cylindrical plasma source has length 60 mm and radius 10 mm. The MN is generated by two rings of permanent magnets which, at the thruster outlet, provide an on-axis strength of $B_0 = 450$ G. The thruster was operated, with xenon at $\dot{m} = 0.2$ mg/s, at total input powers of $P_{in} = 50 - 180$ W. Due to the power drawn by the electronic subsystem, this results in a power delivered to the RF antenna of approximately $P_{RF} = (1 - \epsilon_{sys})P_{in}$, where ϵ_{sys} is the system inefficiency and assumed to be about 0.2. The antenna wave-coupling efficiency is estimated to be $\eta_A \approx 0.7$, so the power actually absorbed into the plasma is $P_a = (1 - \epsilon_{sys})\eta_A P_{in}$.

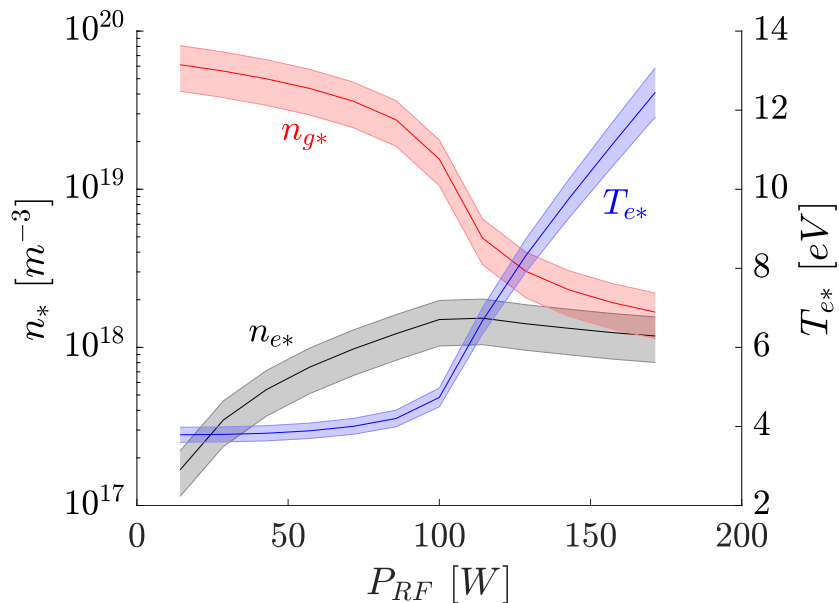


Figure 3. Discharge properties at the source tube exit from the 0D Global Model: electron density n_{e*} (—), neutral density n_{g*} (—), and electron temperature T_{e*} (—)

4.1.2. *Global Model* The 0D Global Model (see Appendix A) was used to obtain the properties of the plasma discharge at the source tube exit. The main parameters (i.e. those that serve as inputs to the PIC model) are given in figure 3 as a function of P_{RF} , where the errorbars are a result of the uncertainty in collision cross sections and sheath assumptions described in reference [26]. Two distinct regions of operation are visible. At <80 W, the electron temperature and neutral gas density are nearly constant, whilst the electron density steadily increases. At around 100 W, there is a transition, and

the neutral density decreases, with electron temperature rapidly increasing. Electron density remains nearly constant, as the neutral-to-plasma ratio approaches unity.

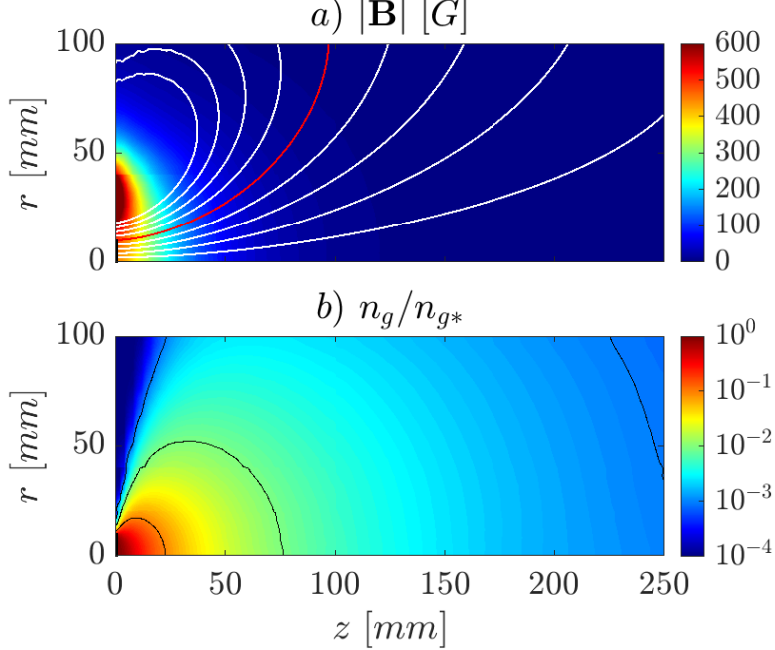


Figure 4. (a) Magnetic field magnitude $|\mathbf{B}|$, the red contour indicates the outermost magnetic field line at the plasma source. (b) Normalised neutral density n_g/n_{g^*} from the DSMC simulation.

4.1.3. PIC model setup The values of n_{e^*} , n_{g^*} and T_{e^*} from the 0D Global Model serve as the inputs to the PIC model as described in section 3. The magnetic topology provided by the permanent magnets is illustrated in 4 (a) on the simulation domain, which spans $L_z = 250$ mm and $L_r = 100$ mm. A piece-wise uniform mesh is used, with $\Delta z = \Delta r = R_0/20 = 0.5$ mm at the thruster outlet, increasing toward the external boundaries. Since $\Delta z \leq \pi\lambda_D$, the value of the artificial permittivity is adjusted to meet this constraint. That is $\gamma = R_0/20\lambda_{D0}$. In this regard, note that it is the ratio of λ_D to the system length scale that is kept constant, not $\tilde{\epsilon}_0$, with the ratio $\tilde{\lambda}_D/R_0 = 20$ given as per the convergence study in [28]. The associated time-step is constrained by the electron Courant-Friedrich-Lewy condition at the maximum T_{e^*} , thus $\Delta t = 0.5\Delta z/(3v_{e,th}) = 1 \times 10^{-10}$ s. Ions and neutrals have a mass scaling of $f = 250$ applied [28]. Since the neutral gas expands geometrically from the thruster, the neutral density field is self-similar across the operating powers; its normalised value is therefore given in figure 4 (b) as computed by the DSMC module of the code. The average number of macro-particles per cell was ensured to be $\hat{N}_p > 50$ per charged species. Finally, the virtual capacitance was set to $C = 0.8$ nF throughout.

Two parameters are varied in the simulations here. Firstly the value of the absorbed power, has been investigated for 30 - 150 W. This is equivalent to altering the neutral-

to-plasma density and electron temperature according to figure 3. Then, the effect of the anomalous transport is analysed by increasing the empirical Bohm parameter α_{an} from 0 (classical) to 0.0625 in the fully-turbulent limit.

4.2. 2D plasma profiles

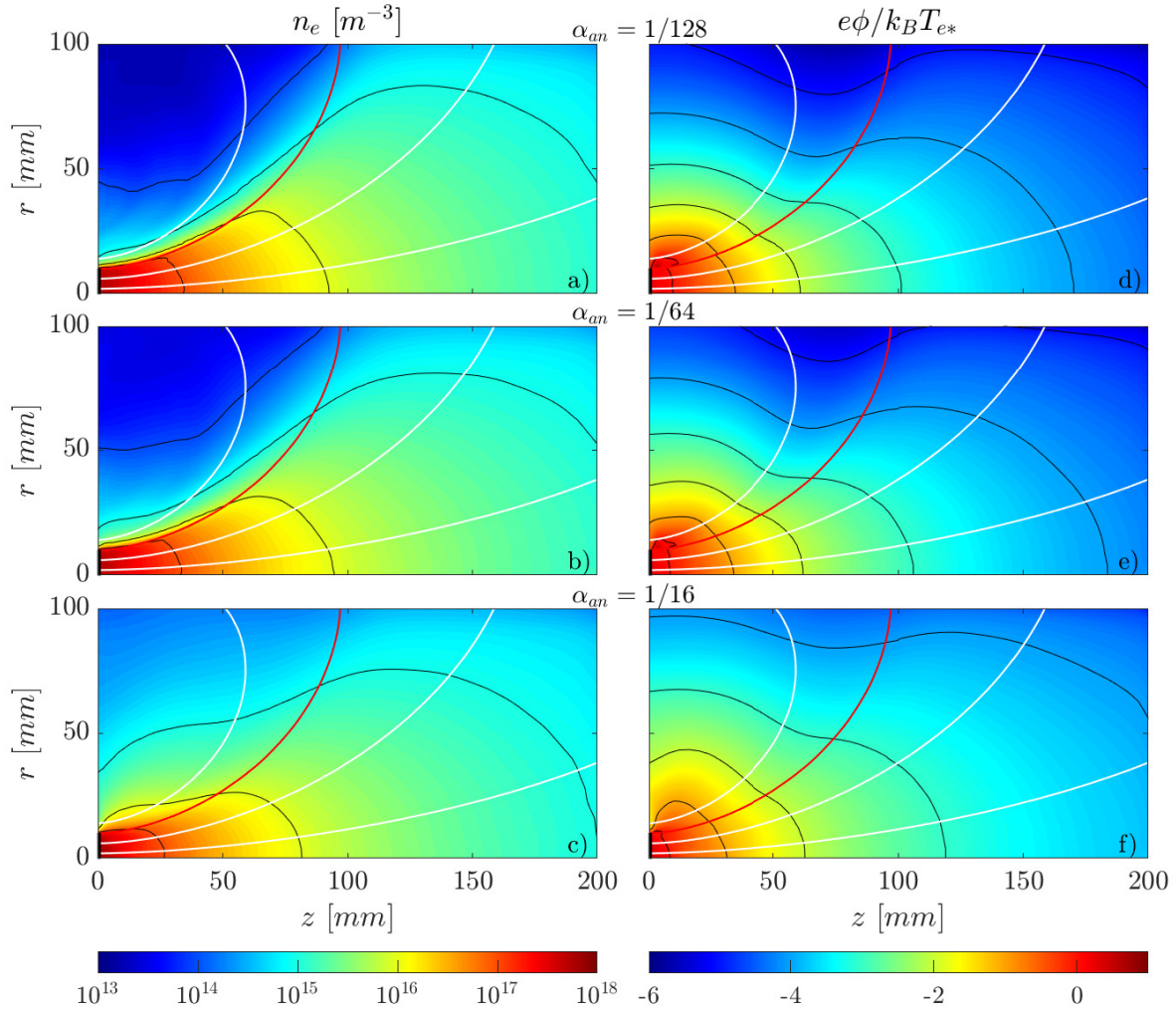


Figure 5. 2D maps of number density n_e and normalised plasma potential $e\phi/k_B T_{e*}$ at $P_a = 30$ W and for $\alpha_{an} = 1/128, 1/64$ and $1/16$.

Figure 5 presents the 2D maps of the electron density n_e and normalised plasma potential $\hat{\phi}$ for the $P_a = 30$ W at three levels of the anomalous parameter α_{an} : $1/128, 1/64$ and $1/16$. Fundamentally, in the axial direction, the plume propagates monotonically downstream under the dominance of the self-consistently developed ambipolar electric field; n_e in the nominal case ($\alpha_{an} = 1/128$) decays two orders of magnitude along the axis due to the plasma beam expansion and acceleration. As expected, the plume is highly-collimated and mostly confined within the boundary of the outermost magnetic field line (OMFL) connected to the plasma source. A dense

region forms just inside the OMFL, which is consistent with the high density conic behaviour found experimentally by Charles [47]. As α_{an} is increased, the collimation is reduced as the plume becomes more weakly-magnetised. In the fully-turbulent limit ($\alpha_{an} = 1/16$), the density decays nearly three orders of magnitude as there is no longer strong radial confinement. The plasma has expanded beyond the OMFL near the plasma source, such that $n_e \approx 10^{15} \text{ m}^{-3}$ in the radial extremum.

Concerning the plasma potential, an ion-confining potential barrier forms along the OMFL at $\alpha_{an} = 1/128$, a phenomena confirmed in other numerical works [42, 43], and found to be enhanced by ion scattering [28]. The peak has a maximum of $0.70T_{e*}$. The structure forms in response to the radial ion energy flux and facilitates their confinement, since the local electric field returns ion trajectories into the MN. It also enhances the transport of electrons towards this magnetically isolated region. At $\alpha_{an} = 1/64$, the potential barrier is inhibited, since the electron transport is instead provided by the anomalous increase in electron cross-field diffusion; the peak reduces to $0.34T_{e*}$. At $\alpha_{an} = 1/16$ the structure is no longer distinguishable; a path of high radial potential, similar to that formed in an unmagnetised case is seen, as the plume follows a more-geometric expansion. This allows the radial flow of ions required by plasma quasineutrality. It will be shown later that the structure of the potential barrier can significantly affect the distributions of the azimuthal electron currents which generate magnetic thrust. From source to infinity, the global potential drop at $\alpha_{an} = 1/128$ is $|\phi_\infty| = 26 \text{ V}$, about $6.8T_{e*}$. The drop lessens significantly as α_{an} increases, as given in table 1. This implies a reduced ion acceleration (and therefore thrust), which will be discussed later.

Table 1. Potential drop at $P_a = 30 \text{ W}$ for increasing α_{an}

α_{an}	1/128	1/64	1/16
$e \phi_\infty /k_B T_{e*}$	6.78	6.50	5.76

4.3. Azimuthal current formation and thrust generation

Figure 6 shows the radial profiles of azimuthal current densities at $z = 2$ and 20 mm for both $P_a = 30$ and 150 W , in which the contributions were calculated as per equation (18); the current densities are normalised by $en_{e*}v_{th,e*}$ (the injected thermal current density). The radial position of the OMFL has also been marked as a vertical dashed line for reference. For each case, the sums of all current density contributions $\hat{j}_{e\theta}$ fit well (error below 1%) with the directly calculated total current density $\hat{j}_{e\theta}^{PIC}$. The friction-induced and inertial currents were found to be small in all cases $j_{e\theta}^{f,M}/j_{e\theta} = \mathcal{O}(10^{-2})$ and thus are omitted for clarity.

At both powers, the magntiude of diamagnetic flow current $\hat{j}_{e\theta}^\chi$ decreases with increasing α_{an} . The maximum intensity of diamagnetic current corresponds to the

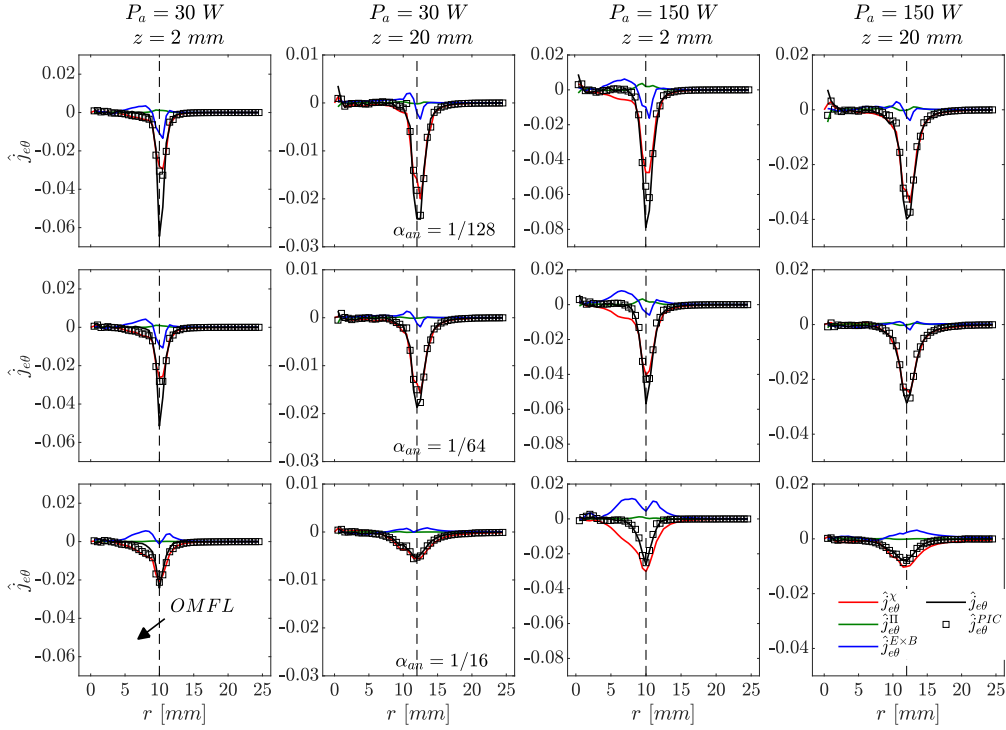


Figure 6. Radial azimuthal current density profiles for $\alpha_{an} = 1/128, 1/64$ and $1/16$ at $P_a = 30$ and 150 W for $z = 2$ and 20 mm. The vertical dashed line indicates the location of the OMFL.

OMFL and, at 2 mm, decreases from -2.9×10^{-2} to -1.2×10^{-2} at 30 W and from -4.7×10^{-2} to -3×10^{-2} at 150 W. The same observations are seen at 20 mm, but the intensity is approximately 60-70% that at 2 mm. This trend is because, at higher α_{an} , there is a weaker plasma confinement along the OMFL, reducing the electron pressure gradient $\partial p_e / \partial r$.

At $1/128$ and $1/64$, the $\mathbf{E} \times \mathbf{B}$ drift currents $\hat{j}_{e\theta}^{E \times B}$ have both a paramagnetic—prior to the OMFL—and diamagnetic contribution—on the OMFL. This is due to aforementioned potential barrier; the plasma potential does not drop monotonically in the radial direction. Rather, it decreases until the OMFL, and rises again to form the potential barrier outside the plume periphery. At $1/16$ however, $\hat{j}_{e\theta}^{E \times B}$ is always paramagnetic. The explanation for this is that the reduced magnetisation leads to the loss of the potential barrier and a higher hall angle (i.e. the angle between the electron current and the magnetic field). Since the expansion approaches the geometric as the cross-field diffusion is high, the electric field is less-aligned with the MN, and thus $\hat{j}_{e\theta}^{E \times B}$ is increased. The paramagnetic current density at 150 W peaks at 1.2×10^{-2} at 2 mm compared to 5.0×10^{-3} at 30 W. This is because the source ions have more energy at higher power (and a number of low-energy ions from in-plume ionisation will be accelerated radially), yielding a greater radial electric field to counter increased ion secondary expansion.

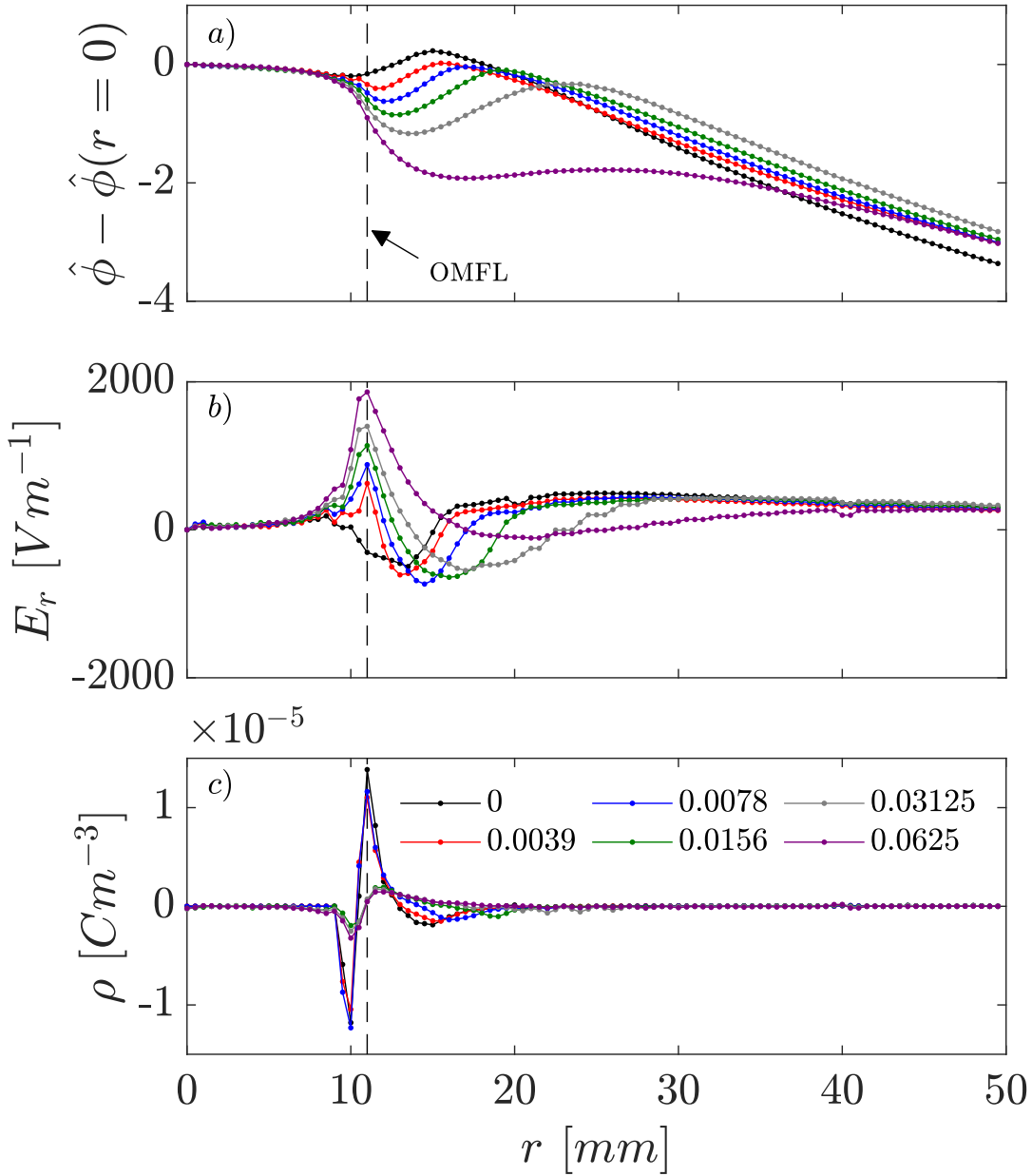


Figure 7. A comparison between the (a) radial plasma potential profiles, (b) radial electric field, and (c) charge density for increasing values of α_{an} in the $P_a = 30$ W case.

As expected the stress-induced current is small $j_{e\theta}^\pi/j_{e\theta} = \mathcal{O}(10^{-1})$ [5]; at 30 W and 1/128, it has a 1.3×10^{-3} maximum at the OMFL at 2 mm, decreasing to negligible at 1/16. The gyrating electrons are exchanged among layers with different macroscopic velocities, leading to a gyration-facilitated viscosity, or inner friction. Therefore, this viscosity will drag the fast layers of plasma flow with the slow ones (and vice-

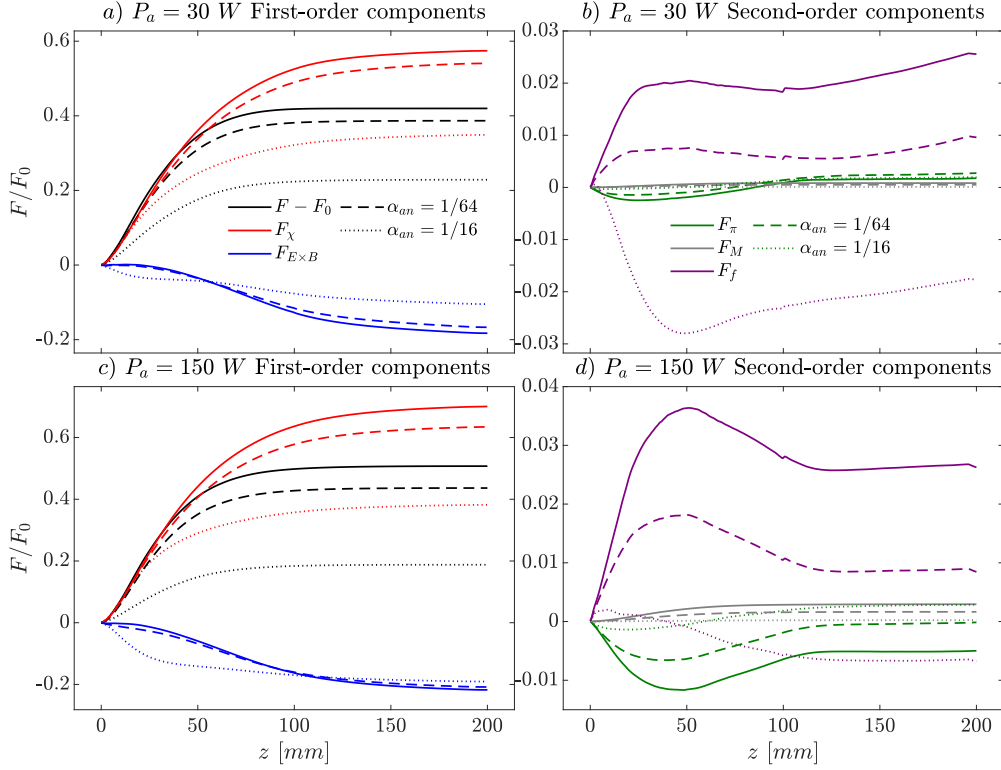


Figure 8. Electromagnetic thrust components accumulating along the MN for 30 W (left) and 100 W (right) and $\alpha = 0$ (top) and $\alpha = 1/16$ (bottom): Total (black line), diamagnetic (red line), $\mathbf{E} \times \mathbf{B}$ (blue line), stress (green line), and friction (grey line).

versa), leading to a macroscopic deceleration/acceleration. In the fully-turbulent case, anomalous collisions act to thermalise the electrons toward an isotropic population, therefore eliminating the viscosity. At 150 W, $j_{e\theta}^\pi$ is generally about 4-times greater than at 30 W, owing to the smaller classical collisionality and so increased effects of electrons drifting radially off the magnetic field lines. Importantly, at 2 mm, $j_{e\theta}^\pi$ is paramagnetic. But, at 20 mm, it becomes diamagnetic. When the electrons start to demagnetise as the magnetic field drops in the downstream, the cyclotron radii of electrons becomes comparable to the system scale and there is an acceleration from the finite electron Larmor radius effect [43].

Further insight is found in figure 7 for six different values of the anomalous parameter α_{an} , where the radial slice at $z = 2$ mm is taken since this is where the plasma potential peak is greatest. It can be seen in figure 7(b) that the potential well coincides with a direction reversal of the radial electric field near the edge of the plasma expansion. In the classical theory, ions with sufficient radial energy near the MN periphery are able to overshoot the edge of the attached electron fluid, and create an excess of positive charge just beyond the boundary, clear in figure 7(c), with a comparable negative charge layer just within the boundary. As α_{an} increases however,

electrons are increasingly able to diffuse across the MN periphery with the ions. This cross-field electron transport balances some of the space-charge and hence dampens the electric field across the OMFL. A potential well of sufficient depth to return the secondary-expanding ions towards the MN can no longer form, and the confinement is greatly diminished as a result. An interesting result of figure 7(c), is a defined transition in the charge density profiles between $\alpha_{an} = 1/128$ and $1/32$. This agrees well with established observations in the literature that there exists a critical condition where a magnetised expansion is collimated, or otherwise under-collimated.

The resultant impact on thrust relies on the volumetric integral of equation (19). By axially truncating the control volume [28], the axial evolution along the MN of the four magnetic thrust components of (21) are given in figure 8 for both $P_a = 30$ W and 100 W. Generally, the diamagnetic flow effect is an accelerating contribution, while $E \times B$ drift induced can be classified as decelerating ones [2]. In all cases, the diamagnetic effect is the dominating term, covering over 90% of positive contribution in each region. The diamagnetic-flow current produced by $\nabla p_e \times \mathbf{B}$ interacts with the applied field, generating a propulsive Lorentz force. In this way, the electron internal energy is converted into the axial kinetic energy of ions. As seen in figure 8s (a) and (c), the diamagnetic thrust is inhibited by the anomalous collisionality by approximately 5% and 40% for $1/64$ and $1/16$ respectively. Increased electron diffusion results in a lower $\partial p_e / \partial \mathbf{1}_\perp$ by weakening the confinement at the OMFL, allowing more plasma to expand beyond the MN. The more-weakly magnetised nozzle therefore has a detachment point shifted upstream, as is clear in the earlier convergence of F_χ in the cases of anomalous diffusion.

The $E \times B$ induced term is the major component of deceleration. The reason for this is the large area of paramagnetic induced currents caused by the inward detachment of ions, determined by the radial electric field that acts in response to the charge separation with the gyrating electrons. At $1/16$, $F_{E \times B}$ is reduced by 70% and 50% for 30 and 150 W respectively in figure 8 (a) and (c). This is since the more weakly confined expansion allows the electron fluid to follow the unmagnetised ions, reducing the magnitude of the radial electric field across the OMFL. An interesting observation however, is that for $\alpha_{an} = 1/16$, this decelerating thrust accumulates rapidly within approximately 50 mm compared to the slow increase in the $1/128$ and $1/64$ cases. Although the decelerating effect of $F_{E \times B}$ is reduced by anomalous effects, it does so less than the comparative reduction in the accelerating F_χ ; the net thrust is reduced by approximately 47% and 62% for 30 and 150 W respectively.

The second-order mechanisms are the stress-induced, inertial and frictional components, which exhibit complex behaviour in figure 8 (b) and (d). First, it is seen that the inertia effect, which converts the directed kinetic energy of electrons to that of the ions, is expectantly small ($F_M < 5 \times 10^{-3} F_0$) due to the tiny mass possessed by electrons. At 30 W, F_π is initially decelerating, but tends to a negligible accelerating contribution at about $z = 100$ mm. At 150 W however, $F_\pi = -5 \times 10^{-2} F_0$ at $1/128$, representing the neoclassical transport that takes place in this less-collisional case. At

1/16 though, $F_\pi = 2.9 \times 10^{-3}F_0$, providing a small positive contribution. Note that the axial distribution of the stress component is insensitive to the anomalous diffusion, only its magnitude. Finally, F_f is the friction-induced force; it is dominated by the anomalous axial and radial collisionalities, which were found to be of order $10^9 - 10^{10}$ Hz and in agreement with the frequencies reported in [25]. At 1/128, $F_f \approx 0.02 - 0.03F_0$ at both powers, so there is a mild transfer of azimuthal momentum to the electrons from collisions and the anomalous axial-radial instabilities. As α_{an} increases to 1/64, $F_f \approx 10^{-2}F_0$. Increased electron diffusion in the plume reduces electron axial drift velocity and increases the radial velocity, with a consequent effect on collisions occurring and F_f .

4.4. Propulsive performance

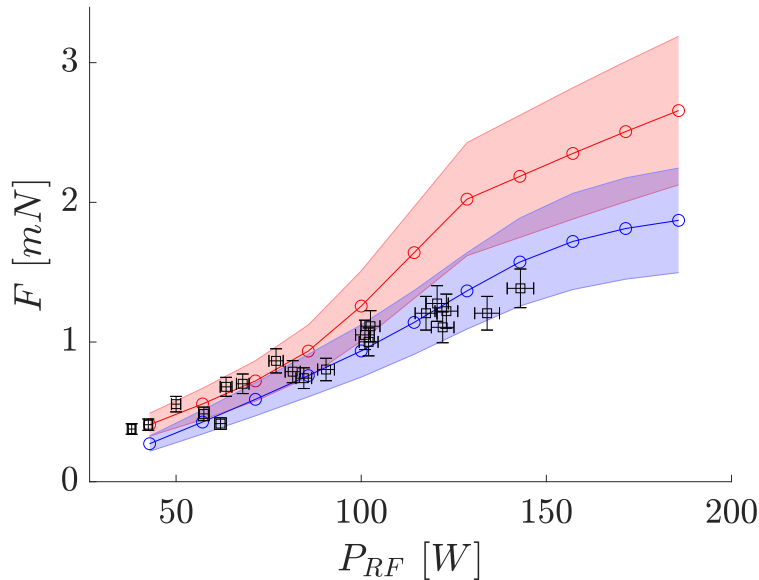


Figure 9. Thrust for $\alpha = 0$ and $\alpha = 1/16$ against experimental measures

Now that the effect of anomalous diffusion on the thrust generation has been concluded in the previous subsection, the scope of the analysis here is to compare, from a macroscopic perspective, the performance with and without anomalous diffusion, and to verify if assuming a fixed value of α_{an} is sufficient to reproduce experimental trends when P_a is varied. A thrust balance, specifically designed for RF thrusters of small-to-medium size was employed as described in [48]. The thrust given by the PIC model is compared to these experimental measures; the results are presented in figure 9 for both the 1/128 and 1/16 cases. There is good agreement in the 1/128 case for $P_{RF} < 80$ W, but at higher powers the thrust is overestimated by up to 48%. This is corrected when anomalous collisions are included, with the experimental points lying within the numerical error. However, at lower powers the 1/128 cases retain the better

fit. This raises questions regarding the dependence of α_{an} on P_{RF} (or more directly P_*). Indeed, the azimuthal fluctuations responsible for anomalous diffusion have been well-documented to be related to the plasma wave energy [21]. This wave energy should be proportional to P_* , thus it is possible that the Bohm coefficient is an increasing function of the thruster power. In addition, a non-negligible background facility pressure may suppress some of the anomalous instability which is presently un-characterised [49]. Regardless, the experimental agreement is within 20%.

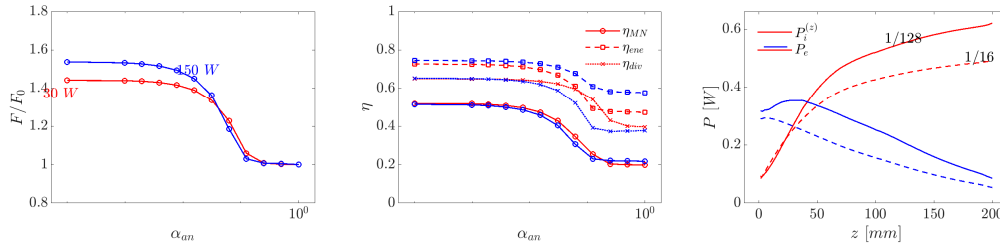


Figure 10. Effect of α_{an} on performance: (a) Thrust gain; (b) Energy, divergence and MN efficiency; (c) Axial evolution of ion and electron power at $P_a = 30$ W.

Further simulations for values of α_{an} between 0 and 1 were carried out, as shown in figure 10 (a) for the MN thrust gain. The anomalous transport becomes negligible (compared with the classical one) for $\alpha_{an} \leq \mathcal{O}(\nu_e/\omega_{ce} \sim 10^{-3})$, with typical values of ν_e about $10^6 - 10^7$ s $^{-1}$ and ω_{ce} about $10^9 - 10^{10}$ s $^{-1}$. The thrust gain diminishes significantly: For 30 and 150 W respectively, F/F_0 decreases from 1.44 and 1.54, when $\alpha_{an} \leq \mathcal{O}(10^{-3})$, towards unity as $\alpha_{an} \geq \mathcal{O}(10^{-1})$. The plume becomes effectively unmagnetised as the anomalous cross-field diffusion inhibits the field-aligned advection of electrons; they can no longer establish sustained gyrations and thus azimuthal current—and therefore magnetic thrust generation—ceases. There is a critical value of α_{an} around 10^{-2} where the thrust loss rapidly increases, and this occurs at lower α_{an} for 150 W; the demagnetised state also occurs earlier for 150 W, at $\alpha_{an} \sim 1/8$ (as opposed to $\alpha_{an} \sim 1/4$ at 30 W). To examine the performance impact in more detail, figure 10 (b) presents the relevant efficiencies. At both 30 and 150 W, the overall MN efficiency η_{MN} decreases from 0.51, aligned with typical values found in other MN simulations [43, 25], to about 0.2. At 150 W, the energy efficiency falls from 0.75 to 0.71 approaching $\alpha_{an} = 1/32$, then undergoes a significant but steady drop to 0.58 for $\alpha_{an} \geq 1/4$. The 30 W case follows a similar trend, but experiences a larger relative loss; η_{ene} drops from 0.73 to 0.47. As discussed in section 4.3, the demagnetisation of electrons reduces the ambipolar potential drop that facilitates energy conversion in the MN. The divergence efficiency η_{div} is around 0.64 for both powers at $\alpha_{an} \leq \mathcal{O}(10^{-2})$, corresponding to an average beam divergence angle of $\cos^{-1}\sqrt{\eta_{div}} \approx 37^\circ$. There is then a very rapid decline toward 0.4 (51°) for $\alpha_{an} \rightarrow 1$, as the magnetic confinement is depleted and the plume approaches a geometric expansion; the transition to this unmagnetised divergence occurs at α_{an} of $1/8$ and $1/2$ for 150 and 30 W respectively.

5. Insight into anomalous electron cooling

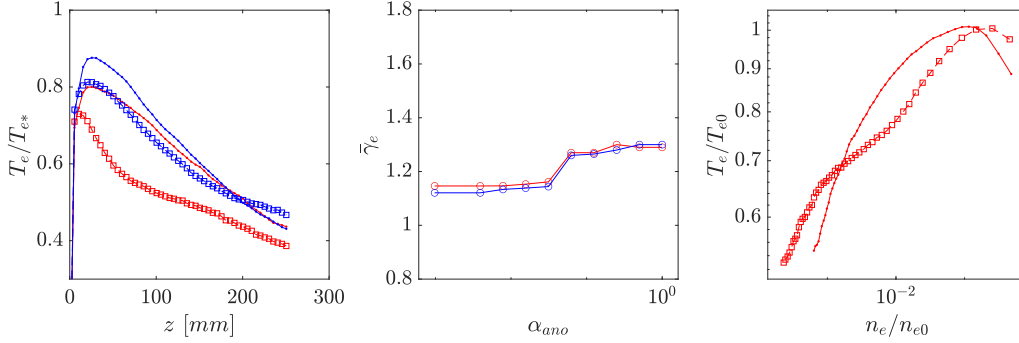


Figure 11. (a) T_e for 43 and 186 W for 0 and 0.0625; (b) polytropic indices for increasing α_{an} ; (c) polytropic fitting.

The anomalous collisions dominate the electron cooling for large values of α (e.g. $\alpha = 1/16$). Figure 11 (a) shows the effect of increasing the anomalous diffusion on the spatial profile of T_e . The slow classical cooling in the upstream region does fit with experimental evidences. As α_{an} increases, the electron cooling also increases and lowers T_e downstream, with a far more rapid decay in the upstream. The inlet temperature (T_{e0}) is also lower for $\alpha = 0.0625$, a product of a smaller potential drop ϕ_∞ which returns less of the full Maxwellian to the plasma source.

Figure 11 (b) provides the corresponding polytropic indices for increasing the anomalous collisionality. A transition occurs between values of 1.16 and 1.29 at $\alpha_{an} = 0.03125$. This confirms what is seen in the conversion efficiency; the plume is no longer magnetised for large values of α_{an} . Figure 11 (c) shows the normalised values of T_e versus n_e in logarithmic scale along the axis. Many experimental and kinetic studies indicate a polytropic relation,

$$\gamma_e = 1 + \frac{\ln T_e/T_{e0}}{\ln n_e/n_{e0}} \quad (33)$$

where γ_e is the fitted polytropic index. Common values for xenon in these studies is 1.15-1.23. With low α the expansion starts near-isothermal and approaches the unmagnetised value of 1.29 downstream once the electrons are detached from the MN. The anomalous diffusion changes the cooling profile significantly. The initial expansion has a $\gamma_e \approx 1.25$ since the electrons are effectively unmagnetised due to the high combination of classical and anomalous collisions. Once the collisionality reduces, the electrons then become partially-magnetised again and $\gamma \approx 1.15$ before undergoing classical detachment, where $\gamma \approx 1.27$.

6. Conclusion

In conclusion, this study demonstrates the significant impact of anomalous diffusion on electron transport and the propulsive performance of magnetic nozzles in low-

power cathode-less RF plasma thrusters through fully kinetic particle-in-cell (PIC) simulations. The results reveal that turbulence-driven non-collisional transport mechanisms, characterized by Bohm-type anomalous collisionality, substantially alter key plasma dynamics. For the REGULUS-150-Xe thruster operating at low (30 W) and high (150 W) power conditions, enhanced cross-field electron transport inhibits the formation of the typical magnetic nozzle potential barrier, reducing radial confinement and lowering the downstream potential drop by up to 15%. This suppression of steep pressure gradients diminishes diamagnetic currents, leaving the $E \times B$ current purely paramagnetic. Consequently, magnetic nozzle efficiency drops from approximately 0.5 to 0.2, driven by reduced electron thermal energy conversion and increased plume divergence. At the Bohm limit of $\omega_{ce}/16$, the simulation achieves agreement with experimental thrust profiles to within 20%, a marked improvement over the 48% overestimation observed in classical models at high power. These findings underscore the importance of accounting for anomalous transport effects in the accurate modeling of plasma thruster performance.

Future work will primarily focus on the proper use of anomalous transport in predictive simulations. This will require the development of a self-consistent model of the anomalous diffusion as a function of the local plasma properties and allowing for behavior varying across both power and mass flow rate regimes. Preliminary work, taking the conjecture that anomalous transport in MNs arises from a kinetic drift-dissipative instability and deriving a self-consistent diffusion from wave quasi-linear theory, has yielded promising results in comparison to experiments [50].

Appendix A. Global Model

A 0D Global (volume-averaged) Model, presented previously in references [26, 51], was adopted to evaluate the plasma properties in the RF source discharge. The dynamics in the source are governed by the species density and energy conservation,

$$\frac{dn'_I}{dt} = Y_{chem}^I - Y_{wall}^I - Y_*^I + Y_{in}^I \quad (\text{A.1})$$

$$\frac{d}{dt} \left(\frac{3}{2} n'_e \bar{T}_e \right) = P_a - P_{chem} - P_{wall} - P_* \quad (\text{A.2})$$

where n'_I is the number density of species I , including excited neutral states. Y_{chem}^I , Y_{wall}^I , Y_*^I and Y_{in}^I are the species I density flux source/sink terms associated to plasma reactions, wall losses, particle outflow, and particle inflow respectively. P_a , P_{chem} , P_{wall} and P_* are the RF power coupled to the plasma, along with the source/sink terms associated to plasma reactions, wall losses, and particle outflow respectively. It should be noted that in these equations $n'_{e,i}$ is the peak plasma density under the RF antenna, whereas n'_g is assumed constant according to the source pressure, and \bar{T}_e is a volume-average.

The plasma reactions considered are electron elastic scattering, ionisation and excitation. Therefore, Y_{chem}^I and P_{chem} are given as

$$Y_{chem}^I = \sum_J K_{IJ} n'_J n'_e - \sum_J K_{JI} n'_I n'_e \quad (\text{A.3})$$

$$P_{chem} = \sum_{I,J} K_{IJ} n'_I n'_e \Delta U_{IJ} + \sum_I K_{II} n'_I n'_e \frac{3m_e}{m_I} \bar{T}_e \quad (\text{A.4})$$

where K_{IJ} is the rate constant for the inelastic transitions from species I to J , K_{II} is the rate constant for elastic collisions between species I and electrons, and ΔU_{IJ} is the energy gap between species I and J .

The Bohm sheath criterion is enforced at the source walls, and with a sonic source tube exit, similar expressions hold for Y_{wall}^I and Y_*^I

$$Y_{wall}^I = \frac{S_{wall}^I}{V} \Gamma_{wall}^I \quad (\text{A.5})$$

$$Y_*^I = \frac{S_*^I}{V} \Gamma_*^I \quad (\text{A.6})$$

where V is the volume of the source, S^I is the equivalent surface area of the source, and Γ^I is the particle flux. For ions and electrons $\Gamma_i = \Gamma_e = n'_e u_B$. Considering the equivalent surface area,

$$S^e = S^i = h_L A_0 + h_R (A_R - A_c) + h_c A_c, \quad (\text{A.7})$$

where h_L , h_R and h_c are the semi-empirical axial, radial and cusp edge-to-centre density ratios respectively. A_R and A_c are the lateral surface area and equivalent area of the cusp loss widths. A full description of these terms is given in reference [51]. For neutrals $Y_{wall}^g = -Y_{wall}^i$, assuming total recombination. The equivalent neutral surface is equal to the source tube exit cross-section, $S_*^g = A_0$ and, assuming the neutrals are in the free-molecular regime, $\Gamma_*^g = 1/4 n'_g \bar{u}_g$.

From the Bohm sheath criterion, the energy terms subsequently read

$$P_{wall,*} = Y_{wall,*}^e \left(2\bar{T}_e \frac{1}{1-\alpha} - 2T_s \frac{\alpha}{1-\alpha} + \phi_{wall,*} \right) \quad (\text{A.8})$$

where α is the secondary electron emission coefficient, T_s is the secondary electron emission temperature and $\phi_{wall,*}$ is the sheath potential given by

$$\phi_{wall,*} = \bar{T}_e \ln \left(\sqrt{\frac{m_i}{2\pi m_e}} (1-\alpha)(1-\delta) \right) \quad (\text{A.9})$$

where δ is the electron elastic reflection coefficient. In the case of the source tube exit, $\alpha = \delta = 0$. For the walls, according to Barra et al. [?], $\delta = \delta_0 E_r^2 / (\bar{T}_e + E_r)^2$ and $\alpha = 2\bar{T}_e / E_s$. The following were assumed in this work: $T_s = 2$ eV, $\delta_0 = 0.4$, $E_r = 20$ eV, and $E_s = 50$ eV.

Regarding the inflow, only neutral gas is injected into the source

$$Y_{in}^g = \frac{\dot{m}}{V m_g} \quad (\text{A.10})$$

where \dot{m} is the propellant mass flow rate.

Given the thruster input power P_{RF} , propellant mass flow rate \dot{m} , and magnetic field \mathbf{B} , the Global Model solves the system of equations to provide \dot{m}_{i^*} , \dot{m}_{g^*} and T_{e^*} to the PIC model,

$$\dot{m}_{i^*} = m_i h_L n'_i u_B A_0 \quad (\text{A.11})$$

$$\dot{m}_{g^*} = m_g n'_g \bar{u}_g A_0 \quad (\text{A.12})$$

$$T_{e^*} = \bar{T}_e \quad (\text{A.13})$$

Acknowledgements

This work was supported by Technology for Propulsion and Innovation (T4i) S.p.A., where REGULUS-150-Xe is currently being developed in the frame of the ESA Contract No.4000130900/20/NL/RA. Acknowledgement is also given to the CINECA award under the ISCRA initiative, for the availability of high-performance computing resources and support.

References

- [1] M. Magarotto, M. Manente, F. Trezzolani, and D. Pavarin, “Numerical model of a helicon plasma thruster,” *IEEE Transactions on Plasma Science*, vol. 48, no. 4, pp. 835–844, 2020.
- [2] E. Ahedo and M. Merino, “Two-dimensional supersonic plasma acceleration in a magnetic nozzle,” *Physics of Plasmas*, vol. 17, no. 7, p. 073501, 2010.
- [3] M. Magarotto, D. Melazzi, and D. Pavarin, “3d-virtus: Equilibrium condition solver of radio-frequency magnetized plasma discharges for space applications,” *Computer Physics Communications*, vol. 247, p. 106953, 2020.
- [4] K. Takahashi, “Helicon-type radiofrequency plasma thrusters and magnetic plasma nozzles,” *Reviews of Modern Plasma Physics*, vol. 3, no. 1, pp. 1–61, 2019.
- [5] Y. Hu, Z. Huang, Y. Cao, and Q. Sun, “Kinetic insights into thrust generation and electron transport in a magnetic nozzle,” *Plasma Sources Science and Technology*, vol. 30, p. 075006, jun 2021.
- [6] S. Di Fede, M. Magarotto, S. Andrews, and D. Pavarin, “Simulation of the plume of a magnetically enhanced plasma thruster with spis,” *Journal of Plasma Physics*, vol. 87, 2021.
- [7] T. Lafleur, “Helicon plasma thruster discharge model,” *Physics of Plasmas*, vol. 21, no. 4, p. 043507, 2014.
- [8] M. Martinez-Sanchez, J. Navarro-Cavallé, and E. Ahedo, “Electron cooling and finite potential drop in a magnetized plasma expansion,” *Physics of Plasmas*, vol. 22, no. 5, p. 053501, 2015.
- [9] N. Bellomo, M. Magarotto, M. Manente, *et al.*, “Design and in-orbit demonstration of regulus, an iodine electric propulsion system,” *CEAS Space Journal*, pp. 1868–2510, 05 2021.
- [10] T. Lafleur, C. Charles, and R. Boswell, “Ion beam formation in a very low magnetic field expanding helicon discharge,” *Physics of Plasmas*, vol. 17, p. 043505, 2010.
- [11] M. Magarotto, D. Melazzi, and D. Pavarin, “Study on the influence of the magnetic field geometry on the power deposition in a helicon plasma source,” *Journal of Plasma Physics*, vol. 85, no. 4, p. 905850404, 2019.
- [12] S. Correyero, J. Jarrige, D. Packan, and E. Ahedo, “Plasma beam characterization along the magnetic nozzle of an ecr thruster,” *Plasma Sources Science and Technology*, vol. 28, p. 095004, 2019.

- [13] M. Magarotto and D. Pavarin, “Parametric study of a cathode-less radio frequency thruster,” *IEEE Transactions on Plasma Science*, vol. 48, no. 8, pp. 2723–2735, 2020.
- [14] N. Souhair, M. Magarotto, S. Dalle Fabbriche, R. Andriulli, S. Andrews, F. Ponti, and D. Pavarin, “Simulation and modelling of an iodine fed helicon plasma thruster,” in *37th International Electric Propulsion Conference*, vol. IEPC-2022-496, (Cambridge, USA), 2022.
- [15] S. Andrews, R. Andriulli, N. Souhair, M. Magarotto, and F. Ponti, “Cathode-less rf plasma thruster design and optimisation for an atmosphere-breathing electric propulsion (abep) system,” *Acta Astronautica*, vol. 225, pp. 833–844, 2024.
- [16] D. Lev *et al.*, “Recent progress in research and development of hollow cathodes for electric propulsion,” *Reviews of Modern Physics*, vol. 3, no. 1, pp. 1–89, 2019.
- [17] M. Manente, F. Trezzolani, M. Magarotto, E. Fantino, A. Selmo, N. Bellomo, E. Toson, and D. Pavarin, “Regulus: A propulsion platform to boost small satellite missions,” *Acta Astronautica*, vol. 157, pp. 241–249, 2019.
- [18] J. M. Little and E. Y. Choueiri, “Electron cooling in a magnetically expanding plasma,” *Phys. Rev. Lett.*, vol. 117, p. 225003, Nov 2016.
- [19] S. Hepner, B. Wachs, and B. Jorns, “Wave-driven non-classical electron transport in a low temperature magnetically expanding plasma,” *Appl. Phys. Lett.*, vol. 116, no. 263502, 2020.
- [20] S. T. Hepner and B. Jorns, “The role of low frequency drift waves in driving non-classical transport in magnetic nozzles,” in *AIAA Propulsion and Energy 2020 Forum*, 08 2020.
- [21] I. D. Kaganovich, A. Smolyakov, Y. Raitses, E. Ahedo, I. G. Mikellides, B. Jorns, F. Taccogna, R. Gueroult, S. Tsikata, A. Bourdon, J.-P. Boeuf, M. Keidar, A. T. Powis, M. Merino, M. Cappelli, K. Hara, J. A. Carlsson, N. J. Fisch, P. Chabert, I. Schweigert, T. Lafleur, K. Matyash, A. V. Khrabrov, R. W. Boswell, and A. Fruchtman, “Physics of $e \times b$ discharges relevant to plasma propulsion and similar technologies,” *Physics of Plasmas*, vol. 27, no. 12, p. 120601, 2020.
- [22] T. Lafleur, R. Martorelli, P. Chabert, and A. Bourdon, “Anomalous electron transport in hall-effect thrusters: Comparison between quasi-linear kinetic theory and particle-in-cell simulations,” *Physics of Plasmas*, vol. 25, no. 6, p. 061202, 2018.
- [23] C. S. Olsen, M. G. Ballenger, M. D. Carter, F. R. C. Díaz, M. Giambusso, T. W. Glover, A. V. Ilin, J. P. Squire, B. W. Longmier, E. A. Bering, and P. A. Cloutier, “Investigation of plasma detachment from a magnetic nozzle in the plume of the vx-200 magnetoplasma thruster,” *IEEE Transactions on Plasma Science*, vol. 43, no. 1, pp. 252–268, 2015.
- [24] N. Souhair, M. Magarotto, F. Ponti, and D. Pavarin, “Analysis of the plasma transport in numerical simulations of helicon plasma thrusters,” *AIP Advances*, vol. 11, p. 115016, 2021.
- [25] A. Sanchez-Villar, J. Zhou, E. Ahedo, and M. Merino, “Coupled plasma transport and electromagnetic wave simulation of an ecr thruster,” *Plasma Sources Science and Technology*, vol. 30, p. 045005, Jan 2021.
- [26] N. Souhair, M. Magarotto, E. Majorana, F. Ponti, and D. Pavarin, “Development of a lumping methodology for the analysis of the excited states in plasma discharges operated with argon, neon, krypton, and xenon,” *Physics of Plasmas*, vol. 28, p. 093504, 2021.
- [27] M. Guaita, M. Magarotto, M. Manente, D. Pavarin, and M. Lavagna, “Semi-analytical model of a helicon plasma thruster,” *IEEE Transactions on Plasma Science*, vol. 50, pp. 425–438, 02 2022.
- [28] S. Andrews, S. D. Fede, and M. Magarotto, “Fully kinetic model of plasma expansion in a magnetic nozzle,” *Plasma Sources Science and Technology*, vol. 31, p. 035022, mar 2022.
- [29] W. van Lynden, N. Souhair, R. Andriulli, M. Magarotto, S. Andrews, A. Cervone, and F. Ponti, “Novel coupling methods for fluid and kinetic solvers in the numerical modeling of helicon plasma thrusters,” in *74th International Astronautical Congress*, no. IAC-23, (Baku, Azerbaijan), 2023.
- [30] F. Cichocki, J. Navarro-Cavallé, A. Modesti, and G. Ramírez Vázquez, “Magnetic nozzle and rpa simulations vs. experiments for a helicon plasma thruster plume,” *Frontiers in Physics*, vol. 10, 2022.
- [31] L. Brieda and M. Keidar, “Development of the starfish plasma simulation code and update on

- multiscale modeling of hall thrusters,” in *48th AIAA/ASME/SAE/ASEE Joint Propulsion Conference & Exhibit*, no. AIAA 2012-4015, (Atlanta, GA, USA), 2012.
- [32] P. Jiménez, M. Merino, and E. Ahedo, “Wave propagation and absorption in a helicon plasma thruster and its plume,” *Plasma Sources Science and Technology*, vol. 31, no. 4, p. 045009, 2022.
- [33] J. Szabo, *Fully kinetic numerical modeling of a plasma thruster*. PhD thesis, Massachusetts Institute of Technology, 07 2001.
- [34] G. A. Bird, *Molecular gas dynamics and the direct simulation of gas flows*. Clarendon: Oxford University press, 1994.
- [35] C. K. Birdsall, “Particle-in-cell charged-particle simulations, plus monte carlo collisions with neutral atoms, pic-mcc,” *IEEE Transactions on Plasma Science*, vol. 19, no. 2, pp. 65–85, 1991.
- [36] A. Guthrie and R. K. Wakerling, *The Characteristics of electrical discharges in magnetic fields*. McGraw-Hill New York, 1st ed. ed., 1949.
- [37] Y. V. Esipchuk and G. N. Tilinin, “Drift instability in a hall-current plasma accelerator,” *Sov. Phys. - Tech. Phys. (Engl. Transl.); (United States)*, vol. 21:4, 4 1976.
- [38] F. F. Chen, *Introduction to plasma physics and Controlled Fusion*, vol. 1. Springer, 1984.
- [39] J. A. Bittencourt, *Fundamentals of Plasma Physics*. Springer Science & Business Media, 2004.
- [40] T. Lafleur, F. Cannat, J. Jarrige, P. Elias, and D. Packan, “Electron dynamics and ion acceleration in expanding-plasma thrusters,” *Plasma Sources Science and Technology*, vol. 24, no. 6, p. 065013, 2015.
- [41] D. M. Goebel and I. Katz, *Fundamentals of electric propulsion: ion and Hall thrusters*. John Wiley & Sons, 2008.
- [42] Z. Chen, Y. Wang, H.-B. Tang, J. Ren, M. Li, Z. Zhe, S. Cao, and J. Cao, “Electric potential barrier in the magnetic nozzle,” *Physical Review E*, vol. 101, p. 053208, 05 2020.
- [43] Z. Chen, Y. Wang, J. Ren, H. Tang, P. Wu, and M. Li, “The fully-kinetic investigations on the ion acceleration mechanisms in an electron-driven magnetic nozzle,” *Plasma Sources Science and Technology*, vol. 31, p. 055013, may 2022.
- [44] M. Duzzi *et al.*, “E-regulus: development of a 150 w prototype of magnetically enhanced plasma thruster,” in *72nd International Astronautical Congress*, no. IAC-19 C4.5.9, (Dubai, UAE), 2021.
- [45] S. Andrews *et al.*, “Multiscale modelling of alternative propellants in helicon plasma thrusters,” in *73 rd International Astronautical Congress*, no. IAC-19 C4.6.9, (Paris, France), 2022.
- [46] S. Andrews, R. Andriulli, N. Souhair, S. Di Fede, M. Magarotto, and F. Ponti, “Coupled global and pic modelling of the regulus cathode-less plasma thrusters operating on xenon, iodine and krypton,” *Acta Astronautica*, vol. 207, pp. 227– 239, 2023.
- [47] C. Charles, “High density conics in a magnetically expanding helicon plasma,” *Applied Physics Letters*, vol. 96, no. 5, p. 051502, 2010.
- [48] T. Trezzolani, M. Magarotto, M. Manente, and D. Pavarin, “Development of a counterbalanced pendulum thrust stand for electric propulsion,” *Measurement*, vol. 122, pp. 494–501, 2018.
- [49] R. Andriulli, S. Andrews, N. Souhair, M. Magarotto, and F. Ponti, “Fully kinetic study of facility pressure effects on rf-source magnetic nozzles,” *Acta Astronautica*, vol. 215, pp. 362– 372, 2024.
- [50] S. Andrews *et al.*, “A self-consistent drift-dissipative instability model of anomalous transport in the magnetic nozzle,” in *38th International Electric Propulsion Conference*, no. IEPC-2024-810, (Toulouse, France), 2024.
- [51] M. Magarotto, S. Di Fede, N. Souhair, S. Andrews, and F. Ponti, “Numerical suite for cathodeless plasma thrusters,” *Acta Astronautica*, vol. 197, pp. 126– 138, 2022.